Title: **A human-ACE2 knock-in mouse model for SARS-CoV-2 infection recapitulates respiratory disorders but avoids neurological disease associated with the transgenic K18-hACE2 model.**

Running title: B.1 SARS-CoV-2 infection of a new hACE-2 Knock-in mice

Anna Pons-Grífols[1], Ferran Tarrés-Freixas[1,2,3,8], Mònica Pérez[2,3], Eva Riveira-Muñoz[1], Dàlia Raïch-Regué[1], Daniel Pérez-Zsolt[1], Jordana Muñoz-Basagoiti[1], Barbara Tondelli[4], Nuria Izquierdo-Useros[1,5,6], Sara Capdevila[7], Júlia Vergara-Alert[2,3], Victor Urrea[1], Jorge Carrillo[1,5,6], Ester Ballana[1,5], Stephen Forrow[4], Bonaventura Clotet[1,8], Joaquim Segalés[2,9], Benjamin Trinité[1,#], Julià Blanco[1,5,6,8,#].

[1]IrsiCaixa, Can Ruti Campus, Badalona, Spain.
[2]Unitat mixta d'investigació IRTA-UAB en Sanitat Animal, Centre de Recerca en Sanitat Animal (CReSA), Campus de la Universitat Autònoma de Barcelona (UAB), Bellaterra, Spain.
[3]IRTA, Programa de Sanitat Animal, Centre de Recerca en Sanitat Animal (CReSA), Campus de la Universitat Autònoma de Barcelona (UAB), Bellaterra, Spain.
[4]Mouse Mutant Core Facility (PBA2B2), Institute for Research in Biomedicine (IRB), Parc Científic de Barcelona, Barcelona, Spain.
[5]Germans Trias i Pujol Research Institute (IGTP), Badalona, Spain.
[6] CIBER Infectious Diseases (CIBERINFEC), Carlos III Health Institute, Madrid, Spain.
[7]Comparative Medicine and Bioimage Centre of Catalonia (CMCiB), Germans Trias i Pujol Research Institute (IGTP), Badalona, Spain.
[8] University of Vic-Central University of Catalonia (UVic-UCC), Vic, Spain.
[9]Departament de Sanitat i Anatomia Animals, Facultat de Veterinària, Universitat Autònoma de Barcelona (UAB), Campus de la UAB, Bellaterra, Spain.

 # Corresponding authors

Benjamin Trinité: btrinite@irsicaixa.es

Julià Blanco: jblanco@irsicaixa.es

JS, BT and JB are co-senior authors

Abstract Word count: 245

Text word count: 4955

Abstract

Animal models have been instrumental in elucidating the pathogenesis of SARS-CoV-2 infection and testing COVID-19 vaccines and therapeutics. Wild-type (WT) mice are not susceptible to many SARS-CoV-2 variants, therefore transgenic K18-hACE2 mice have emerged as a standard model system. However, this model is characterized by severe disease, particularly associated with neuroinfection, which leads to early humane endpoint euthanasia. Here, we established a novel knock-in (KI) mouse model by inserting the original K18-hACE2 transgene into the collagen COL1A1 locus using a recombinase mediated cassette exchange (RMCE) system. Once the Col1a1-K18-hACE2 mouse colony was established, animals were challenged with a B.1 SARS-CoV-2 (D614G) isolate and were monitored for up to 14 days. Col1a1-K18-hACE2 mice exhibited an initial weight loss similar to the K18-hACE2 transgenic model but did not develop evident neurologic clinical signs. The majority of Col1a1-K18-hACE2 mice did not reach the preestablished humane endpoint, showing progressive weight gain after 9 days post-infection (dpi). Importantly, despite this apparent milder pathogenicity compared to the K18-hACE2 transgenic model, high levels of viral RNA were detected in lungs, oropharyngeal swab, and nasal turbinate. Conversely, in sharp contrast to K18-hACE2 transgenic mice, no viral replication was detected in the brains of Col1a1-K18-hACE2 animals at any timepoint, explaining the reduced severity of clinical signs. At 14 dpi, while infection was cleared in the lungs, increased lesions and residual inflammation were detected. Overall, Col1a1-K18-hACE2 mice constitute a new model for investigating SARS-CoV-2 pathogenesis and treatments, with potential implications for studying long-term COVID-19 sequelae.

58 **Importance**

59 K18-hACE2 mice express high levels of the human protein ACE-2, the receptor for SARS-
60 CoV-2, and therefore are infected by this virus. These animals have been crucial to
61 understand viral pathogenesis and to test COVID-19 vaccines and antiviral drugs.
62 However, K18-hACE2 rapidly die after infection with initial SARS-CoV-2 variants due to
63 a massive brain infection that does not occur in humans. Here, we used a technology
64 known as knock-in that allows for the targeted insertion of a gene into a mouse and we
65 have generated a new hACE2-mouse. We have characterized this new animal model
66 demonstrating that the virus replicates in the respiratory tract, damaging and inflaming
67 the lungs; however, in contrast to K18-hACE2 mice, no brain infection was observed,
68 and most animals recovered from infection. This new model could be instrumental for
69 the study of specific disease aspects such as post-COVID condition, sequelae, and
70 susceptibility to reinfection.

71

72 **Keywords:** animal model, lung inflammation, lung damage, neuroinvasion, post covid
73 condition.

74

75

76

77 **Introduction**

78 Severe Acute Respiratory Syndrome Coronavirus 2 (SARS-CoV-2) is the etiologic agent of the
79 coronavirus disease 2019 (COVID-19). The COVID-19 pandemic fuelled an unprecedented
80 collaborative research effort to develop therapeutics and vaccines. Animal models that
81 recapitulate key clinical and pathological features of COVID-19 have played a pivotal role in
82 testing novel vaccines, antivirals and other treatments (1).

83 The spike glycoprotein of SARS-CoV-2 uses the angiotensin-converting enzyme 2 (ACE2) as
84 receptor to enter and infect host cells (2). ACE2 is expressed on the surface of cells of
85 different organs such as lungs, intestine, kidneys, and heart. However, the spike
86 glycoprotein from ancestral SARS-CoV-2 strains does not efficiently bind to mouse ACE2
87 (mACE2), rendering wild-type (WT) mice refractory to infection. Therefore, several
88 strategies were used to develop mouse models susceptible to infection. These strategies
89 include viral adaptation (3) or the introduction of the human ACE2 (hACE2) receptor via viral
90 vectors and transgenic approaches (4–8).

91 Both K18-hACE2 transgenic mice and Golden Syrian hamsters (GSH) became reference
92 animal models for investigating SARS-CoV-2 pathogenesis in vivo. They mainly differ in
93 pathogenesis: GSH, which are naturally susceptible to SARS-CoV2 infection, recapitulate a
94 milder disease phenotype (1). The transgenic mouse model was originally developed for the
95 study of SARS-CoV, which also targets human ACE2. It was created by random insertion of
96 multiple copies of the *hACE2* gene under the control of the human cytokeratin 18 gene
97 promoter (*KRT18* or K18). This promoter allows for high-level expression and is specific to
98 epithelial cells, including those in the airways (9, 10). This approach allows the infection of

99 mice by SARS-CoV-2, while maintaining the activity of the mACE2 receptor. Infection of K18-
100 hACE2 mice with pre-Omicron variants of SARS-CoV-2 courses with progressive weight-loss
101 and strong clinical signs by 3-5 days post-infection (dpi), a severity which requires
102 euthanasia by 5-7 dpi. The lethality in this model is dose- and SARS-CoV-2 variant-
103 dependent (10, 11), and has been associated with neuroinvasion and extensive brain
104 infection (McCray et al., 2007; Carossino et al., 2022; Tarrés-Freixas et al., 2022; Vidal et al.,
105 2022). Neuroinvasion in K18-hACE2 transgenic mice has been linked to the aleatory gene
106 insertion and the high number of inserted gene copies, around 8 in the commercial *B6.Cg-*
107 *Tg(K18-ACE2)2Prlmn/J-K18-hACE2 mouse* (https://www.jax.org/strain/034860), leading to
108 altered expression levels and tissue distribution of the receptor (15). Specifically, a higher
109 number of gene copies correlates with a worse disease prognosis and encephalitis in this
110 model, following SARS-CoV infection (16). These neurological lesions are not consistent with
111 the pathology of COVID-19 in humans, where infection of the central nervous system was
112 not observed at such level (17). Therefore, new animal models that better recapitulate the
113 human disease, without viral neuroinvasion, should be developed.

114 Knock-in (KI) models are characterized by the targeted insertion of a defined gene copy
115 number in a specific locus, therefore providing a more predictable expression of the
116 transgene. In this work, we used a recombinase-based approach to insert the original K18-
117 hACE2 transgene into the collagen type I alpha chain (COL1A1) locus to generate a Col1a1-
118 K18-hACE2 KI mouse. To characterize this new model, mice were challenged with a SARS-
119 CoV-2 B.1 (D614G) isolate and pathogenicity was compared with the well-characterized

120 K18-hACE2 transgenic mice. After viral challenge of a Col1a1-K18-hACE2 mice, we
121 confirmed viral replication and lesions in the lungs, but absence of viral neuroinvasion.
122

123 **Results**

124 **Characterization of hACE2 expression in the Col1a1-K18-hACE2 mice**

125 We generated a new hACE2 KI mouse model through addition of the original K18-hACE2
126 transgene, kindly supplied by Paul McCray (9) at the COL1A1 locus using a recombinase
127 mediated system (**Figure 1A**) (18). Traditional transgenic techniques rely on the random
128 genomic insertion of an unpredictable number of transgene copies. This frequently results
129 in a highly variable level and pattern of transgene expression, due to cis acting regulatory
130 elements at the site of insertion. A single copy of a transgene, inserted into the well
131 characterised Col1A1 locus, is expected to result in a more predictable level and pattern of
132 expression of the transgene sequence. To confirm the correct expression of the transgene
133 in this KI model, we quantified *hACE2* transcripts relative to the house-keeping gene GAPDH
134 by RT-qPCR in RNA samples extracted from twelve different tissues. Additionally, the same
135 analysis was performed in K18-hACE2 mice to compare both models. Expression of the
136 hACE2 transgene in K18-hACE2 mice was similar among most tested tissues except in
137 muscle and heart, which showed lower values (**Figure 1B).** In contrast, hACE2 expression in
138 Col1a1-K18-hACE2 mice was more heterogenous, with the lowest expression observed in
139 the brain and liver. When comparing the relative expression of hACE2 between both
140 models, we observed higher expression in the pancreas, lymph nodes and muscle of Col1a1-
141 K18-hACE2 mice. Conversely, in the kidney, brain and liver, expression was higher in the
142 K18-hACE2 mouse model. Minor differences were observed in the rest of the analyzed
143 tissues (**Figure 1C**).

144 **Survival of Col1a1-K18-hACE2 mice following SARS-CoV-2 B.1 infection**.

145 Col1a1-K18-hACE2 mice (n=27) and K18-hACE2 mice (n=4) were challenged intranasally
146 with a SARS-CoV-2 B.1 (D614G) isolate. Uninfected KI animals, used as a control, received
147 an intranasal dose of PBS (n=5). Animal weight and clinical signs were monitored daily for
148 14 days after infection. The endpoints to collect samples were set at 3-, 7-, and 14-days
149 post-infection (dpi, n=8 Col1a1-K18-hACE2 mice per endpoint) or upon fulfilment of
150 humane endpoint criteria (**Figure 2A**).

151 Both animal models started losing weight around 3 dpi, consistent with previous studies
152 with B.1 isolates in transgenic animals (**Figure 2B**) (13). In K18-hACE2 transgenic animals,
153 the decrease in weight was associated with a dramatic increase of clinical signs: mobility,
154 dyspnoea, and neurological effects (Supplementary Table 1). This severity fulfilled the
155 humane endpoint criteria, leading to euthanasia of all K18-hACE animals by 6 or 7dpi (**Figure**
156 **2C**). In contrast, while Col1a1-K18-hACE2 mice underwent weight loss, they did not show
157 severe clinical signs apart from a slight decrease in activity. Three Col1a1-K18-hACE2
158 animals had to be euthanized (exitus) due exclusively to a weight-loss exceeding the 20%
159 limit (humane endpoint) at 8, 9 and 10 dpi. But interestingly, all other KI animals started to
160 regain weight after 9 dpi, reaching 90% of their initial weight by 14 dpi (**Figure 2B/C**). These
161 results indicate that B.1 SARS-CoV-2 infection in Col1a1-K18-hACE2 mice is significantly less
162 lethal compared to k18-hACE2 transgenic mice (**Figure 2C**).

163 To explore the extent of viral infection in both animal models, viral loads (VL, cell-free viral
164 RNA) were quantified in a large set of samples (oropharyngeal swabs, lung, brain, nasal
165 turbinate, muscle, intestine, liver, kidney, pancreas, salivary glands, lymph nodes and
166 spleen) collected from a subset of animals (n=20). Respiratory tract tissues showed

167 detectable VL in both models, while the brain showed high VL exclusively in K18-ACE2
168 transgenic samples. In both models, VL were mostly undetected in all other tissues except
169 for low levels found in the heart and salivary glands (**Supplementary Figure 1**).

170 **B.1 replicates in the respiratory tract of Col1a1-K18-hACE2 KI mice.**

171 To fully characterize the kinetics of viral replication in the respiratory tract, samples from
172 oropharyngeal swab, lung, and nasal turbinate were collected at 3, 7, and 14 dpi or at the
173 humane endpoint (exitus) in all Col1a1-K18-hACE2 mice. Samples from K18-hACE2
174 transgenic mice obtained at euthanasia (6 and 7 dpi) were used as references. Virological
175 analysis in oropharyngeal swab, lung, and nasal turbinate revealed widespread infection in
176 both K18-hACE2 and Col1a1-K18-hACE2 mice in all mentioned tissues across two
177 independent experiments (**Figure 3A**). VL in the nasal turbinate were similar in both animal
178 models, with some viral RNA still detected at 14 dpi in Col1a1-K18-hACE2 mice. RNA levels
179 in oropharyngeal swabs and lung peaked at 3 dpi in Col1a1-K18-hACE2 mice and tended to
180 decay overtime up to 14 dpi. Col1a1-K18-hACE2 animals euthanized at the humane
181 endpoint at 8-10 dpi still displayed high viral RNA in lungs, which could explain their more
182 pronounced weight-loss and early fulfilment of endpoint criteria. To further confirm viral
183 clearance, titration of replication-competent virus was performed in lung samples. Similar
184 to the VL kinetics, viral titers peaked at 3 dpi, followed by a quick and significant decrease
185 (**Figure 3B,** 3 dpi vs 7 dpi: p = 0.00178).

186 To further characterize viral pathogenesis, formalin-fixed lung samples from both animal
187 models were analyzed by histology and immunohistochemistry (IHC) to score the presence

188 of lesions and SARS-CoV-2 antigen (nucleoprotein, NP), respectively. Histological lesions
189 were semi-quantified as none, mild, moderate, or severe (score 0-3), and the detection of
190 viral antigen as lack, low, moderate, or high (score 0-3). In Col1a1-K18-hACE2 KI mice,
191 histopathological analysis showed an increase in lung lesion average overtime, reaching a
192 maximum score of two at 14 dpi in most animals **(Figure 3C and D).** IHC detection of SARS-
193 CoV-2 NP in the lungs of Col1a1-K18-hACE2 KI mice was consistent with the VL analyses,
194 showing the highest score early upon infection (3 dpi). Antigen detection decreased with
195 time showing apparent clearance by 14 dpi **(Figure 3C and D).**

196 To assess infection-driven inflammation, the levels of IP-10, IL-6, IFNγ, MCP-1 and MIP-1β
197 were measured by Luminex in lung samples from both animal models at the indicated
198 timepoints. While all cytokines were increased in infected animals, compared to uninfected
199 controls, IP-10 and IL-6 showed a longitudinal dynamic comparable to viral load and IHC
200 data in Col1a1-K18-hACE2 KI mice, peaking at 3 dpi and significantly decreasing by 14 dpi
201 (**Figure 4**). In contrast, IFNγ, MCP-1, and MIPβ peaked at 7 dpi and decayed afterwards,
202 although no statistical differences were observed among the analyzed timepoints. Overall,
203 levels of inflammatory mediators at 7 dpi in Col1a1-K18-hACE2 KI mice were comparable to
204 K18-hACE2 transgenic mice at the time of euthanasia.

205 **Col1a1-K18-hACE2 KI mice do not develop brain infection.**

206 To investigate the discrepancy in VL observed in the brain (**Supplementary Figure 1**) and
207 the differences in survival and clinical signs observed between each model (**Figure 2C**), we
208 performed a longitudinal virological and histological analysis of brain samples. VL were

209 detected at low levels in only 2 out of 8 Col1a1-K18-hACE2 KI mice analyzed at 7 dpi and
210 importantly, no VL was found in animals reaching the humane endpoint. In contrast, all K18-
211 hACE2 brain samples showed high VL at euthanasia (6-7dpi) (**Figure 5A**). Similar results were
212 obtained when formalin-fixed brain samples were analyzed for histopathology and IHC,
213 scored in a blinded fashion as described above. Histopathological analysis of the brain in the
214 Col1a1-K18-hACE2 model showed no lesions at any of the analyzed timepoints. In contrast,
215 brain samples from K18-hACE2 infected animals showed lesion scores of 2 and 1 **(Figure 5B**
216 **and C).** Furthermore, no detection of SARS-CoV-2 NP in the brain of Col1a1-K18-hACE2 mice
217 was observed by IHC at any timepoint or at the humane endpoint, while K18-hACE2 mice
218 showed a high density of antigen diffused throughout the tissue (score 3) at euthanasia
219 **(Figure 5C).** Brain lesions in the transgenic model were characterized as multifocal
220 lymphoplasmacytic meningoencephalitis and were observed alongside the detection of
221 viral antigen in the brain (**Figure 5C**).

222

223 **Discussion**

224 In this study, we characterized a novel hACE2 KI murine model by evaluating the course of
225 infection with the B.1 D614G SARS-CoV-2 variant with a direct comparison to the well-
226 described K18-hACE2 transgenic mouse model, in which this variant is known to be highly
227 pathogenic. The most relevant findings included the susceptibility of the KI model to SARS-
228 CoV-2 infection and the reduced lethality imputed to the absence of viral replication and
229 lesions in the brain.

230 The development of this KI model was started at the beginning of the COVID-19 pandemic
231 as an alternative to the K18-hACE2 transgenic mouse model. Even though the transgenic
232 model had already been established and used in previous SARS-CoV studies (9), the
233 availability of these animals was limited at first, as colonies needed to be restarted from
234 cryopreserved embryos. In this context, several laboratories developed new hACE2 murine
235 models for SARS-CoV-2 infection. Expression of the hACE2 transgene was achieved through
236 various methods, including directed insertion using CRISPR/Cas9 technology (19) using
237 different promoters such as Hepatocyte nuclear factor-3/forkhead homologue 4 (Hfh4)
238 promoter (20) or the mouse ACE2 promoter (6), and by infecting mice with replication-
239 defective adenovirus encoding hACE2 (3). In this work, we followed a different strategy
240 wherein a single copy of the transgene was inserted into the COL1A1 locus, but under the
241 K18 promoter as the original transgenic K18-hACE2 model. The selection of this locus was
242 based on its known ability to provide reliable and ubiquitous expression of inserted
243 sequences (18). Additionally, RMCE allowed the insertion of a single transgene copy which
244 should better mimic physiological expression, potentially impacting lethality through

245 reduction of the ectopic expression and modification of tissue distribution of the hACE2
246 receptor. A recent study identifying a correlation between lower hACE2 copy number and
247 reduced pathology further supports our initial hypothesis (21).

248 When comparing with K18-hACE2 transgenic mice, B.1 infection of the new Col1a1-K18-
249 hACE2 KI mouse model resulted in much less severe clinical signs with better responsiveness
250 and physical appearance and no neurological sign. These observations were consistent with
251 a lack of detectable viral replication in brain of Col1a1-K18-hACE2 KI mice, as summarised
252 in **Figure 6**. Focusing on the respiratory tract, viral replication was observed in both models,
253 although VL and antigen detection were in general lower at 7 dpi in Col1a1-K18-hACE2 KI
254 mice. In contrast, lung tissue lesions and inflammation were fully comparable in both
255 models at this timepoint (**Figure 6**).

256 To explain the different behaviour between each model, hACE2 expression was analyzed in
257 different tissues. While expression in the lungs and nasal turbinates was comparable, the
258 brain and liver showed lower expression of hACE2 in Col1a1-K18-hACE2 KI mice. This finding
259 better mimics the physiological distribution in humans, where hACE2 expression in the brain
260 is low (22). Expression of mACE2 was not analyzed, as mice are not susceptible to the B.1
261 variant through the murine receptor, and no changes in their levels or distribution were
262 expected compared to WT mice (15, 23). Among the clinical parameters analyzed in Col1a1-
263 K18-hACE2 KI infected mice, we found that initial weight-loss was similar to that of the K18-
264 hACE mice but was not accompanied by the increased severity of clinical signs that
265 characterizes infection in these transgenic mice (neurological signs, lack of responsiveness,
266 and poor general appearance) (13). Consistent with this observation, infection of Col1a1-

267 K18-hACE2 KI mice coursed with a partial recovery in weight by 14 dpi in most animals.
268 Importantly, the survival rate of Col1a1-K18-hACE2 KI mice was over 70%, with the three
269 deaths exclusively due to a weight loss of more than 20%, which was one of the humane
270 endpoints in our study.

271 Among the tissues analyzed in Col1a1-K18-hACE2 KI infected mice, we found significant
272 replication of SARS CoV-2 in the respiratory tract, mainly in the lungs. Despite viral clearance
273 in Col1a1-K18-hACE2 KI mice which was confirmed by viral titration and IHC, lung lesions
274 were similar between both models by 7dpi and remained after 14 dpi in KI animals
275 recovering from the infection. The impact of viral replication in lungs, on local expression of
276 inflammatory markers, was also confirmed and found to be comparable to the inflammation
277 profile reported in K18-hACE2 transgenic mice (24, 25). Infection of Col1a1-K18-hACE2 KI
278 mice induced higher levels of IFN-g, IL-6, IP-10, MCP-1 and MIP-1b cytokines. The
279 longitudinal analysis showed early impact on IL-6 and IP-10 levels (3 dpi) and a clear trend
280 to normalization by 14 dpi, with some residual inflammation remaining. This is consistent
281 with the presence of lesions at this timepoint, and the immune cell infiltration described by
282 21 dpi in K18-hACE2 transgenic mice surviving infection (25).

283

284 The main difference between the Col1a1-K18-hACE2 KI and the K18-hACE2 transgenic
285 models was found in neuroinvasion. Only residual levels of viral RNA were detected in the
286 brains of Col1a1-K18-hACE2 KI mice. Furthermore, no detectable brain lesions, such as the
287 multifocal lymphoplasmacytic meningoencephalitis reported in K18-hACE2 transgenic mice
288 (14) were detected by histology. A complete absence of SARS-CoV-2 nucleoprotein in the

289 brain was evidenced by IHC. Importantly, the three animals that reached humane endpoints
290 did not present any evidence of brain viral replication but showed enhanced lung infection.
291 These observations are consistent with the lower level of hACE2 expression in the brain of
292 Col1a1-K18-hACE2 KI compared to the K18-hACE2 transgenic animals. Therefore, the
293 targeted insertion of the hACE2 transgene seems to be a crucial factor leading to lower
294 levels of brain infection and neurological clinical signs. However, different studies have
295 shown that neuroinvasion is only partially dependent on the expression of hACE2 receptor
296 (12), and that both delivery route and viral dose can also play a role in the magnitude of the
297 neuroinvasion (22, 26). In our case, to exclusively analyze the effect of receptor expression,
298 we kept the intranasal administration route and $TCID_{50}$ dose established and characterized
299 in our own and others' studies to ensure comparability of the results (13).

300 Our study is a preliminary characterization of a new animal model and has consequently
301 several limitations. First, the expression of hACE-2 in different tissues has only been
302 analyzed at the mRNA level, with no data on immunohistochemistry to confirm the
303 presence of the protein. Moreover, we have focused on the characterization of one viral
304 variant and a single dose. The B.1 (D614G) variant was selected for its demonstrated
305 severity in K18-hACE2 mice and its inability to use mACE2 as an entry receptor, unlike
306 B.1.351/Beta and BA1.1/Omicron variants (13, 15). While ancestral and earlier variants
307 (B.1.1.7/Alpha, B.1.351/Beta B.1.617.2/Delta) were highly pathogenic in K18-hACE2 mice,
308 BA.1.1/Omicron caused a milder infection with no weight loss nor neuroinvasion, therefore
309 reducing lethality in this model (13). However, more recent Omicron subvariants such as
310 BQ.1.1, BA.5 and XBB.1.5 appear to be regaining pathogenicity in K18-hACE2 mice (27–29).

311 Increased lung infection, pro-inflammatory cytokines, and lung pathology are observed with
312 these variants, with data on neuroinvasion and neurovirulence on the latter (29). Further
313 characterization of the latest variants in the KI model would provide relevant insights into
314 the full impact of the KI insertion of the transgene and confirm the suitability of this model
315 for the study of both ancestral and emerging variants. Nevertheless, for the B.1 SARS-CoV-
316 2 variant it shows similarity with GSH in viral dynamics and pathology, with no
317 neuroinvasion. This new model, however, has the upside of a wider reagent availability,
318 scarce in GSH (1), and easier animal facility allowance.

319 In summary, several mouse models for the evaluation of antivirals and vaccines have been
320 developed to date, with disease phenotypes ranging from mild to severe COVID-19-like
321 condition. None of these models, however, can fully recapitulate all aspects of the disease
322 as it occurs in humans. The development and further characterization of new animal
323 models, like the Col1a1-K18-hACE2 model, may overcome some of these limitations and
324 provide valuable tools to study certain aspects of COVID-19. Survival of Col1a1-K18-hACE2
325 KI mice after infection with a highly pathogenic variant could provide a model which better
326 mimics human disease progression, and thus could be instrumental for the study of specific
327 disease aspects such as post-COVID condition (PCC), sequelae, long-term effects of drug
328 therapies, and susceptibility to reinfection.

329 **Materials and methods**

330 **Creation of the Knock-in Model**

331 A new KI mouse model, **B6;129S-Col1a1$^{tm1(K18\text{-}hACE2)Irb}$/Irsi** (Col1a1-K18-hACE2), was created
332 by inserting the original K18-hACE2 transgene into the collagen COL1A1 locus using a

333 recombinase-mediated cassette exchange (RMCE) FLP-FRT system in KH2 cells (18). The
334 actual insertion site lies approximately 0.3 kb downstream of the 3'UTR end of COL1A1. As
335 such, the inserted transgene remains identical to the original designed one (9) and the
336 hACE2 cDNA is under the control of the K18 promoter rather than COL1A1. Specifically, the
337 plasmid PGK-ATG-Frt was digested with EcoRV, and the sequence
338 ATCAGACGTCGCTAGCGGCGCGCCGGTACTAGT was inserted to create a multi-cloning site.

339 The plasmid containing hACE2 under the control of the K18 promoter (K18-hACE2), supplied
340 by Paul McCray, was digested with HpaI and XbaI enzymes. The resulting transgene
341 fragment was isolated and purified, and then cloned into the EcoRV-NheI sites of the
342 modified PGK-ATG-Frt plasmid to generate the targeting vector. The targeting vector was
343 then co-transfected with an Flp expression construct into KH2 cells by electroporation. The
344 cells were then placed under hygromycin selection for 9 days, after which drug resistant
345 colonies were picked, expanded, and screened for the presence of the targeted transgene.
346 Once confirmed, the modified embryonic stem cells were injected into mouse blastocysts.
347 These injected mouse blastocysts were then placed into recipient foster females via embryo
348 transfer techniques.

349 **Biosafety Approval and Virus Isolation**

350 The execution of SARS-CoV-2 experiments was approved by the biologic biosafety
351 committee of Germans Trias i Pujol Research Institute (IGTP) and performed at the Biosafety
352 Level 3 laboratory (BSL-3) of the Comparative Medicine and Bioimage Centre (CSB-20-015-
353 M8; CMCiB, Badalona, Spain).

354 The B.1 SARS-CoV-2 isolate used in this study was isolated from nasopharyngeal swabs of
355 hospitalized patients in Spain as described elsewhere (30, 31). Briefly, viruses were
356 propagated in Vero E6 cells (CRL-1586; ATCC, Virginia, VA, United States) for two passages
357 and recovered by supernatant collection. The sequence of the SARS-CoV-2 variant tested is
358 deposited at the GISAID Repository with accession IDs EPI_ISL_510689. EPI_ISL_510689 was
359 the first SARS-CoV-2 virus isolated in Catalonia in March 2020 and, compared to the Wuhan/
360 Hu-1/2019 (WH1) strain, this isolate had the S protein mutations D614G, which is associated
361 with the B.1 lineage, and R682L. Viral stocks were titrated on Vero E6 cells to use equivalent
362 TCID50/mL using the Reed-Muench method and sequential 1/10 dilutions of the viral stocks
363 as described previously (31).

364 **Animal Procedures and Study Design**

365 All animal procedures were approved by the Committee on the Ethics of Animal
366 Experimentation of the IGTP and were authorized by the *Generalitat de Catalunya* (code:
367 11222). All animal experiments followed the principles of animal welfare and the 3Rs. All
368 experiments and sample processing were performed inside the BSL-3 facility. Col1a1-K18-
369 hACE2 hemizygous KI mice were produced and bred at Parc Científic de Barcelona (PCB) by
370 pairing hemizygous males for Tg(K18-ACE2)2Prlmn (or K18-hACE2) with non-carrier
371 C57Bl6/J females. Animals used as control, B6.Cg-Tg(K18-ACE2)2Prlmn/J (or K18-hACE2)
372 hemizygous transgenic mice (034860, Jackson Immunoresearch, West Grove, PA, United
373 States) were bred at CMCiB in the Specific Pathogen Free Area (SPF) by pairing hemizygous
374 K18-hACE2 males with non-carrier C57Bl6/J females. The genotype of the offspring
375 regarding both K18-hACE2 and Col1a1-K18-hACE2 mice was determined by qPCR at the

376 IGTP's Genomics Platform from tail samples. Both animal models were kept in the BSL-3
377 facility during the whole experiment including acclimatization period. The housing
378 conditions in the BSL-3 room were maintained as follows: a temperature of 22±2ºC,
379 humidity levels between 30-70%, 20 ACH, a 12h dark/light cycle, and access to food and
380 water *ad libitum.*

381 A total of 36 adult mice aged 5-11 months were used in this experiment, consisting of 32 KI
382 Col1a1-K18-hACE2 mice and 4 transgenic K18-hACE2 mice. All groups were sex balanced.
383 The infections were performed in two separate experiments between January and June
384 2022. Mice were anaesthetized with isoflurane (FDG9623; Baxter, Deerfield, IL, USA) and
385 infected with a B.1 isolate (27 Col1a1-K18-hACE2 and 4 K18-hACE2 mice). The uninfected
386 control group received PBS (5 Col1a1-K18-hACE2).

387 Infection was performed using 1,000 $TCID_{50}$ of B.1 SARS-CoV-2 isolate in 50 µl of PBS (25
388 µl/nostril), or PBS only (25 µl/nostril) for the control group. All mice fully recovered from
389 the challenge and anaesthesia procedures. Following the challenge, body weight and clinical
390 signs were monitored daily. Eight animals per group were euthanized at days 3, 7, 14 dpi or
391 upon fulfilment of human endpoint, for viral RNA quantification and histopathological
392 analyses (**Supplementary Table 2**). The endpoint criteria for animal welfare were
393 established based on a body weight loss superior to 20% of the initial body weight and/or
394 the display of moderate to severe clinical signs (including neurological signs), in accordance
395 with previous studies (12–14). Categories evaluated included respiration, physical
396 appearance, lack of responsiveness and neurological changes, that were scored from 0-2
397 depending on severity. Euthanasia was performed under deep isoflurane anaesthesia by

398 whole blood extraction via cardiac puncture and was confirmed by cervical dislocation.
399 Oropharyngeal swab, lung, brain, and nasal turbinate were collected for viral RNA
400 quantification, histological and ICH analyses. For the latter techniques, tissues were fixed
401 by immersion in 10% buffered formalin. An additional set of 9 tissues was collected to
402 further characterize the KI model both for viral RNA quantification and hACE2 receptor
403 expression. These tissues included muscle, intestine, liver, kidney, lymph nodes, spleen,
404 heart, pancreas, and salivary glands.

405 **hACE2 Receptor Tissue Expression**

406 Several samples from both KI and transgenic models were collected and processed to
407 analyze potential differences in hACE2 receptor expression. These samples included
408 oropharyngeal swab, lung, brain, nasal turbinate, muscle, intestine, liver, kidney, pancreas,
409 salivary glands, lymph nodes, and spleen. Tissues were processed with a TissueLyser II
410 (85,300; QIAGEN) for further VL quantification, and transgene expression was analyzed by
411 RT-qPCR analysis.

412 **SARS-CoV-2 PCR Detection and Viral Load Quantification**

413 Viral RNA was quantified by RT-PCR in both the standard set of samples (oropharyngeal
414 swab, lung, brain, and nasal turbinate), and the extended set (muscle, intestine, liver,
415 kidney, pancreas, salivary glands, lymph nodes and spleen). The collected tissues were
416 processed, and VL determined as described by Tarrés-Freixas et al. 2022 (13). Briefly,
417 approximately 100 mg of each tissue was collected in 1.5 mL Sarstedt tubes (72,607;
418 Sarstedt, Nümbrecth, Germany) containing 500 µl of DMEM medium (11,995,065;
419 ThermoFisher Scientific) supplemented with 1% penicillin–streptomycin (10,378,016;

420 ThermoFisher Scientific, Waltham, MA, United States). A 1.5 mm Tungsten bead (69,997;
421 QIAGEN, Hilden, Germany) was added to each tube, and samples were homogenized twice
422 at 25 Hz for 30 s using a TissueLyser II (85,300; QIAGEN) before being centrifuged for 2 min
423 at 2,000 × g. Supernatants were then stored at −80°C until analysis.

424 RNA extraction was performed by using the Viral RNA/ Pathogen Nucleic Acid Isolation kit
425 (A42352, ThermoFisher Scientific), optimized for use with a KingFisher instrument
426 (5,400,610; ThermoFisher Scientific), following the manufacturer's instructions. PCR
427 amplification was based on the 2019-Novel Coronavirus Real-Time RT-PCR Diagnostic Panel
428 guidelines and protocol developed by the American Center for Disease Control and
429 Prevention (CDC-006-00019, v.07). Briefly, a 20 µL PCR reaction was set up containing 5 µl
430 of RNA, 1.5 µL of N2 primers and probe (2019-nCov CDC EUA Kit, catalogue number
431 10,006,770, Integrated DNA Technologies, Coralville, IA, USA) and 10 µl of GoTaq 1-Step RT-
432 qPCR (Promega, Madison, WI, USA). Thermal cycling was performed at 50°C for 15 min for
433 reverse transcription, followed by 95°C for 2 min and then 45 cycles of 95°C for 10 s, 56°C
434 for 15 s and 72°C for 30 s in the Applied Biosystems 7,500 or QuantStudio5 Real-Time PCR
435 instruments (ThermoFisher Scientific). For absolute quantification, a standard curve was
436 built using 1/5 serial dilutions of a SARS-CoV-2 plasmid (2019-nCoV_N_Positive Control,
437 catalog number 10006625, 200 copies/µL, Integrated DNA Technologies), which was run in
438 parallel with all PCR determinations. Viral RNA from each sample was quantified in
439 triplicate, and the mean viral RNA concentration (in copies/mL) was extrapolated from the
440 standard curve and corrected by the corresponding dilution factor. Mouse *gapdh* gene

441 expression was measured in duplicate for each sample using TaqMan®gene expression
442 assay (Mm99999915_g1; ThermoFisher Scientific) as amplification control.

443 **Viral Titration**

444 Lung tissues were evaluated for the presence of replicative virus by titration in Vero E6 cells
445 as previously described (14, 31, 32). Briefly, after tissue homogenization, each sample
446 underwent sequential 10-fold dilutions in duplicate, transferred onto a monolayer of Vero
447 E6 cell in a 96-well plate, and incubated at 37°C and 5% CO_2. Plates were monitored daily
448 under a microscope, and at 5 dpi, wells were evaluated for the presence of cytopathic
449 effects. The amount of infectious virus was calculated by determining the TCID50 using the
450 Reed–Muench method.

451 **Histopathological and Immunohistochemical Analyses**

452 Tissue samples were recovered at the designated endpoint (3,7,14 dpi or exitus) and fixed
453 by immersion in 10% buffered formalin. Lung, nasal turbinate, and brain samples were
454 routinely processed for histopathological examination, with haematoxylin & eosin-stained
455 slides examined under an optical microscope in a blinded fashion. A semi-quantitative
456 approach based on the amount of inflammation (none, mild, moderate, or severe) was used
457 to assess the damage caused by SARS-CoV-2 infection in mice, following a previously
458 published scoring system (14, 33). Additionally, an IHC technique was employed to detect
459 SARS-CoV-2 NP antigen in nasal turbinate, lung, and brain sections from all animals, using a
460 rabbit monoclonal antibody (40143-R019, Sino Biological, Beijing, China) at a 1:15,000
461 dilution. The amount of viral antigen in tissues was semi-quantitatively scored in a blinded
462 fashion (low, moderate, and high amount, or lack of antigen detection) (14, 33).

463 **Cytokine quantification**

464 To assess the viral-driven inflammation in lung in both animal models, the levels of IP-10,
465 IL-6, IFNγ, MCP-1 and MIP-1β cytokines were analyzed by Luminex in tissue extracts. Lung
466 samples were processed as stated in the VL quantification section and stored at -80ºC until
467 analysis. In Col1a1-K18-hACE2 mice, cytokines were analyzed at 3,7,14 dpi and those
468 euthanized by humane endpoint criteria (exitus). Uninfected Col1a1-K18-hACE2 and K18-
469 hACE2 infected animals were used as reference groups.

470 Cytokines were measured by Luminex xMAP technology and analyzed with xPONENT 3.1
471 software (Luminex Corporation) using the MCYTOMAG-70 kit, according to the
472 manufacturers' protocol with minor modifications. Briefly, after staining the desired
473 cytokines, samples underwent an overnight incubation on a rocking shaker at 4°C, using 2%
474 PFA to ensure complete inactivation of any remaining SARS-CoV-2 particles; a fixation that
475 does not alter cytokine quantification (34). Before plate acquisition, the PFA was washed
476 away and replaced with sheath fluid.

477 **Statistical Analyses**

478 All figures were generated using GraphPad Prism 9.0.0. Statistical analyses were performed
479 using R v4.3. Survival Rates were estimated with Kaplan-Meier curves and compared with
480 the Log-rank test. Datasets with an abundance of data below the limit of detection, like VL,
481 were analyzed using the Peto-Peto Left-censored samples test with correction for multiple
482 comparisons. Histopathological, IHC scores and viral titrations were compared using an
483 Independence Asymptotic Generalized Pearson Chi-Squared Test for ordinal data. Cytokine
484 titers were compared by a Kruskal Wallis, with pairwise comparisons conducted using
485 Conover's non-parametric test.

486

487

Acknowledgements

The authors would like to acknowledge Jorge Díaz, Yaiza Rosales-Salgado, Rosa María Ampudia-Carrasco, Sergi Sunyé-Casas and Mireia Martínez from the CMCiB for their essential help in the BSL3 facility and the K18-hACE2 mouse colony. We also thank Marisa Larramona from Parc Científic de Barcelona for her unvaluable help with the knock-in mouse colony. We thank the Dormeur Fondation for their financial support for the acquisition of the QuantStudio-5 real-time PCR system.

Author Contributions

AP-G, FT-F, BTrinité, and JB conceived and designed the experiments. AP-G, FT-F, and BTrinité performed the animal procedures. AP-G, FT-F, MP, ER-M, DR-R, DP-Z, JM-B, JS, BT performed the analytical experiments. AP-G, BTrinité, JS, JV-A, VU and JB analyzed and interpreted the data. SF, BTondelli established and provided the Knock-in mouse colony. SC established communication between animal facilities and contributed to the veterinary report verification to allow the knock-in animal shipment to the CMCiB facility. DP-Z, JM-B, DR-R, NI-U provided key reagents. AP-G, BT, and JB wrote the paper. All authors contributed to the article and approved the submitted version.

Competing Interests /Funding

A.P-G was supported by a predoctoral grant from Generalitat de Catalunya and Fons Social Europeu (2022 FI_B 00698). This study was funded by Grifols, the Departament de Salut of the Generalitat de Catalunya (grant nos. SLD016 to J.B. and SLD015 to J.C.), the Spanish Health Institute Carlos III, CERCA Programme/Generalitat de Catalunya 2021 SGR 00452, and the crowdfunding initiatives #joemcorono, BonPreu/Esclat, and Correos. NI-U is

510 supported by the Spanish Ministry of Science and Innovation (grant PID2020-117145RB-I00
511 and 10.13039/501100011033, Spain), EU HORIZON-HLTH-2021CORONA-01 (grant
512 101046118, European Union) and by institutional funding of Pharma Mar, Grifols, HIPRA,
513 and Amassence. J. Blanco has received institutional funding from Grífols, Nesapor Europe,
514 HIPRA and MSD. Unrelated to the submitted work, J.B. and J.C. are founders and
515 shareholders of AlbaJuna Therapeutics, SL. B.C. is founder and shareholder of AlbaJuna
516 Therapeutics, SL, and AELIX Therapeutics, SL.

517 The funders had no role in study design, data collection and interpretation, or the decision
518 to submit the work for publication

519 **Data availability**

520 The data supporting the findings of this study are documented within the paper and are
521 available from the corresponding authors upon request.

522

523

524 **References**

525 1. Muñoz-Fontela C, Dowling WE, Funnell SGP, Gsell PS, Riveros-Balta AX, Albrecht RA,
526 Andersen H, Baric RS, Carroll MW, Cavaleri M, Qin C, Crozier I, Dallmeier K, de Waal
527 L, de Wit E, Delang L, Dohm E, Duprex WP, Falzarano D, Finch CL, Frieman MB,
528 Graham BS, Gralinski LE, Guilfoyle K, Haagmans BL, Hamilton GA, Hartman AL,
529 Herfst S, Kaptein SJF, Klimstra WB, Knezevic I, Krause PR, Kuhn JH, Le Grand R, Lewis
530 MG, Liu WC, Maisonnasse P, McElroy AK, Munster V, Oreshkova N, Rasmussen AL,
531 Rocha-Pereira J, Rockx B, Rodríguez E, Rogers TF, Salguero FJ, Schotsaert M,
532 Stittelaar KJ, Thibaut HJ, Tseng C Te, Vergara-Alert J, Beer M, Brasel T, Chan JFW,
533 García-Sastre A, Neyts J, Perlman S, Reed DS, Richt JA, Roy CJ, Segalés J, Vasan SS,
534 Henao-Restrepo AM, Barouch DH. 2020. Animal models for COVID-19. Nature
535 586:509–515.

536 2. Jackson CB, Farzan M, Chen B, Choe H. 2021. Mechanisms of SARS-CoV-2 entry into
537 cells. Nat Rev Mol Cell Biol 2021 231 23:3–20.

538 3. Hassan AO, Case JB, Winkler ES, Thackray LB, Kafai NM, Bailey AL, McCune BT, Fox
539 JM, Chen RE, Alsoussi WB, Turner JS, Schmitz AJ, Lei T, Shrihari S, Keeler SP,
540 Fremont DH, Greco S, McCray PB, Perlman S, Holtzman MJ, Ellebedy AH, Diamond
541 MS. 2020. A SARS-CoV-2 Infection Model in Mice Demonstrates Protection by
542 Neutralizing Antibodies. Cell 182:744-753.e4.

543 4. Tseng C-TK, Huang C, Newman P, Wang N, Narayanan K, Watts DM, Makino S,
544 Packard MM, Zaki SR, Chan T, Peters CJ. 2007. Severe Acute Respiratory Syndrome
545 Coronavirus Infection of Mice Transgenic for the Human Angiotensin-Converting
546 Enzyme 2 Virus Receptor. J Virol 81:1162–1173.

547 5. Jiang R Di, Liu MQ, Chen Y, Shan C, Zhou YW, Shen XR, Li Q, Zhang L, Zhu Y, Si HR,
548 Wang Q, Min J, Wang X, Zhang W, Li B, Zhang HJ, Baric RS, Zhou P, Yang X Lou, Shi
549 ZL. 2020. Pathogenesis of SARS-CoV-2 in Transgenic Mice Expressing Human
550 Angiotensin-Converting Enzyme 2. Cell 182:50-58.e8.

551 6. Bao L, Deng W, Huang B, Gao H, Liu J, Ren L, Wei Q, Yu P, Xu Y, Qi F, Qu Y, Li F, Lv Q,
552 Wang W, Xue J, Gong S, Liu M, Wang G, Wang S, Song Z, Zhao L, Liu P, Zhao L, Ye F,
553 Wang H, Zhou W, Zhu N, Zhen W, Yu H, Zhang X, Guo L, Chen L, Wang C, Wang Y,
554 Wang X, Xiao Y, Sun Q, Liu H, Zhu F, Ma C, Yan L, Yang M, Han J, Xu W, Tan W, Peng
555 X, Jin Q, Wu G, Qin C. 2020. The pathogenicity of SARS-CoV-2 in hACE2 transgenic
556 mice. Nat 2020 5837818 583:830–833.

557 7. Zhou B, Thao TTN, Hoffmann D, Taddeo A, Ebert N, Labroussaa F, Pohlmann A, King
558 J, Steiner S, Kelly JN, Portmann J, Halwe NJ, Ulrich L, Trüeb BS, Fan X, Hoffmann B,
559 Wang L, Thomann L, Lin X, Stalder H, Pozzi B, de Brot S, Jiang N, Cui D, Hossain J,
560 Wilson MM, Keller MW, Stark TJ, Barnes JR, Dijkman R, Jores J, Benarafa C,
561 Wentworth DE, Thiel V, Beer M. 2021. SARS-CoV-2 spike D614G change enhances
562 replication and transmission. Nature 592:122–127.

563 8. Winkler ES, Chen RE, Alam F, Yildiz S, Case JB, Uccellini MB, Holtzman MJ, Garcia-
564 Sastre A, Schotsaert M, Diamond MS. 2022. SARS-CoV-2 Causes Lung Infection
565 without Severe Disease in Human ACE2 Knock-In Mice. J Virol 96.

566 9. McCray PB, Pewe L, Wohlford-Lenane C, Hickey M, Manzel L, Shi L, Netland J, Jia HP,
567 Halabi C, Sigmund CD, Meyerholz DK, Kirby P, Look DC, Perlman S. 2007. Lethal
568 Infection of K18- hACE2 Mice Infected with Severe Acute Respiratory Syndrome
569 Coronavirus . J Virol 81:813–821.

570 10. Zheng J, Wong LYR, Li K, Verma AK, Ortiz ME, Wohlford-Lenane C, Leidinger MR,
571 Knudson CM, Meyerholz DK, McCray PB, Perlman S. 2021. COVID-19 treatments
572 and pathogenesis including anosmia in K18-hACE2 mice. Nature 589:603–607.

573 11. Winkler ES, Bailey AL, Kafai NM, Nair S, McCune BT, Yu J, Fox JM, Chen RE, Earnest
574 JT, Keeler SP, Ritter JH, Kang LI, Dort S, Robichaud A, Head R, Holtzman MJ,
575 Diamond MS. 2020. SARS-CoV-2 infection of human ACE2-transgenic mice causes
576 severe lung inflammation and impaired function. Nat Immunol 2020 2111 21:1327–
577 1335.

578 12. Carossino M, Kenney D, O'connell AK, Montanaro P, Tseng AE, Gertje HP, Grosz KA,
579 Ericsson M, Huber BR, Kurnick SA, Subramaniam S, Kirkland TA, Walker JR, Francis
580 KP, Klose AD, Paragas N, Bosmann M, Saeed M, Balasuriya UBR, Douam F, Crossland
581 NA. 2022. Fatal Neurodissemination and SARS-CoV-2 Tropism in K18-hACE2 Mice Is
582 Only Partially Dependent on hACE2 Expression. Viruses 2022:535.

583 13. Tarrés-Freixas F, Trinité B, Pons-Grífols A, Romero-Durana M, Riveira-Muñoz E,
584 Ávila-Nieto C, Pérez M, Garcia-Vidal E, Perez-Zsolt D, Muñoz-Basagoiti J, Raïch-
585 Regué D, Izquierdo-Useros N, Andrés C, Antón A, Pumarola T, Blanco I, Noguera-
586 Julián M, Guallar V, Lepore R, Valencia A, Urrea V, Vergara-Alert J, Clotet B, Ballana
587 E, Carrillo J, Segalés J, Blanco J. 2022. Heterogeneous Infectivity and Pathogenesis of
588 SARS-CoV-2 Variants Beta, Delta and Omicron in Transgenic K18-hACE2 and
589 Wildtype Mice. Front Microbiol 13.

590 14. Vidal E, López-Figueroa C, Rodon J, Pérez M, Brustolin M, Cantero G, Guallar V,
591 Izquierdo-Useros N, Carrillo J, Blanco J, Clotet B, Vergara-Alert J, Segalés J. 2022.
592 Chronological brain lesions after SARS-CoV-2 infection in hACE2-transgenic mice.
593 Vet Pathol 59:613–626.

594 15. Shuai H, Chan JF-W, Yuen TT-T, Yoon C, Hu J-C, Wen L, Hu B, Yang D, Wang Y, Hou Y,
595 Huang X, Chai Y, Chan CC-S, Poon VK-M, Lu L, Zhang R-Q, Chan W-M, Ip JD, Chu AW-
596 H, Hu Y-F, Cai J-P, Chan K-H, Zhou J, Sridhar S, Zhang B-Z, Yuan S, Zhang AJ, Huang J-
597 D, To KK-W, Yuen K-Y, Chu H. 2021. Emerging SARS-CoV-2 variants expand species
598 tropism to murines. EBioMedicine 73:103643.

599 16. Netland J, Meyerholz DK, Moore S, Cassell M, Perlman S. 2008. Severe Acute
600 Respiratory Syndrome Coronavirus Infection Causes Neuronal Death in the Absence
601 of Encephalitis in Mice Transgenic for Human ACE2. J Virol 82:7264–7275.

602 17. Meinhardt J, Streit S, Dittmayer C, Manitius R v., Radbruch H, Heppner FL. 2023. The
603 neurobiology of SARS-CoV-2 infection. Nat Rev Neurosci 2023 251 25:30–42.

604 18. Beard C, Hochedlinger K, Plath K, Wutz A, Jaenisch R. 2006. Efficient method to
605 generate single-copy transgenic mice by site-specific integration in embryonic stem
606 cells. Genesis 44:23–28.

607 19. Sun SH, Chen Q, Gu HJ, Yang G, Wang YX, Huang XY, Liu SS, Zhang NN, Li XF, Xiong R,
608 Guo Y, Deng YQ, Huang WJ, Liu Q, Liu QM, Shen YL, Zhou Y, Yang X, Zhao TY, Fan CF,
609 Zhou Y Sen, Qin CF, Wang YC. 2020. A Mouse Model of SARS-CoV-2 Infection and
610 Pathogenesis. Cell Host Microbe 28:124-133.e4.

611 20. Jiang R Di, Liu MQ, Chen Y, Shan C, Zhou YW, Shen XR, Li Q, Zhang L, Zhu Y, Si HR,
612 Wang Q, Min J, Wang X, Zhang W, Li B, Zhang HJ, Baric RS, Zhou P, Yang X Lou, Shi
613 ZL. 2020. Pathogenesis of SARS-CoV-2 in Transgenic Mice Expressing Human
614 Angiotensin-Converting Enzyme 2. Cell 182:50-58.e8.

615 21. Bradshaw CM, Georgieva T, Tankersley TN, Taylor- T, Johnson L, Uhrlaub JL,
616 Besselsen D, Janko Ž. 2023. Characterization of low copy number human
617 angiotensin- converting enzyme 2 (hACE2) -transgenic mice as an improved model
618 of SARS-CoV-2 infection 2.

619 22. Dong W, Mead H, Tian L, Park J-G, Garcia JI, Jaramillo S, Barr T, Kollath DS, Coyne
620 VK, Stone NE, Jones A, Zhang J, Li A, Wang L-S, Milanes-Yearsley M, Torrelles JB,
621 Martinez-Sobrido L, Keim PS, Barker BM, Caligiuri MA, Yu J. 2022. The K18-Human
622 ACE2 Transgenic Mouse Model Recapitulates Non-severe and Severe COVID-19 in
623 Response to an Infectious Dose of the SARS-CoV-2 Virus. J Virol 96.

624 23. Gembardt F, Sterner-Kock A, Imboden H, Spalteholz M, Reibitz F, Schultheiss HP,
625 Siems WE, Walther T. 2005. Organ-specific distribution of ACE2 mRNA and
626 correlating peptidase activity in rodents. Peptides 26:1270–1277.

627 24. Oladunni FS, Park JG, Pino PA, Gonzalez O, Akhter A, Allué-Guardia A, Olmo-
628 Fontánez A, Gautam S, Garcia-Vilanova A, Ye C, Chiem K, Headley C, Dwivedi V,
629 Parodi LM, Alfson KJ, Staples HM, Schami A, Garcia JI, Whigham A, Platt RN, Gazi M,
630 Martinez J, Chuba C, Earley S, Rodriguez OH, Mdaki SD, Kavelish KN, Escalona R,
631 Hallam CRA, Christie C, Patterson JL, Anderson TJC, Carrion R, Dick EJ, Hall-Ursone S,
632 Schlesinger LS, Alvarez X, Kaushal D, Giavedoni LD, Turner J, Martinez-Sobrido L,
633 Torrelles JB. 2020. Lethality of SARS-CoV-2 infection in K18 human angiotensin-
634 converting enzyme 2 transgenic mice. Nat Commun 11.

635 25. Yinda CK, Port JR, Bushmaker T, Owusu IO, Purushotham JN, Avanzato VA, Fischer
636 RJ, Schulz JE, Holbrook MG, Hebner MJ, Rosenke R, Thomas T, Marzi A, Best SM, de
637 Wit E, Shaia C, van Doremalen N, Munster VJ. 2021. K18-hACE2 mice develop
638 respiratory disease resembling severe COVID-19. PLOS Pathog 17:e1009195.

639 26. Fumagalli V, Ravà M, Marotta D, Di Lucia P, Laura C, Sala E, Grillo M, Bono E,
640 Giustini L, Perucchini C, Mainetti M, Sessa A, Garcia-Manteiga JM, Donnici L,

641 Manganaro L, Delbue S, Broccoli V, De Francesco R, D'Adamo P, Kuka M, Guidotti
642 LG, Iannacone M. 2022. Administration of aerosolized SARS-CoV-2 to K18-hACE2
643 mice uncouples respiratory infection from fatal neuroinvasion. Sci Immunol 7.

644 27. Case JB, Scheaffer SM, Darling TL, Bricker TL, Adams LJ, Harastani H, Trende R,
645 Sanapala S, Fremont DH, Boon ACM, Diamond MS. 2023. Characterization of the
646 SARS-CoV-2 BA.5.5 and BQ.1.1 Omicron Variants in Mice and Hamsters. bioRxiv
647 Prepr Serv Biol 2023.04.28.538747.

648 28. Halfmann PJ, Iida S, Iwatsuki-Horimoto K, Maemura T, Kiso M, Scheaffer SM, Darling
649 TL, Joshi A, Loeber S, Singh G, Foster SL, Ying B, Case JB, Chong Z, Whitener B,
650 Moliva J, Floyd K, Ujie M, Nakajima N, Ito M, Wright R, Uraki R, Warang P, Gagne M,
651 Li R, Sakai-Tagawa Y, Liu Y, Larson D, Osorio JE, Hernandez-Ortiz JP, Henry AR,
652 Ciuoderis K, Florek KR, Patel M, Odle A, Wong LYR, Bateman AC, Wang Z, Edara VV,
653 Chong Z, Franks J, Jeevan T, Fabrizio T, DeBeauchamp J, Kercher L, Seiler P,
654 Gonzalez-Reiche AS, Sordillo EM, Chang LA, van Bakel H, Simon V, Alburquerque B,
655 Alshammary H, Amoako AA, Aslam S, Banu R, Cognigni C, Espinoza-Moraga M,
656 Farrugia K, van de Guchte A, Khalil Z, Laporte M, Mena I, Paniz-Mondolfi AE,
657 Polanco J, Rooker A, Sominsky LA, Douek DC, Sullivan NJ, Thackray LB, Ueki H,
658 Yamayoshi S, Imai M, Perlman S, Webby RJ, Seder RA, Suthar MS, García-Sastre A,
659 Schotsaert M, Suzuki T, Boon ACM, Diamond MS, Kawaoka Y. 2022. SARS-CoV-2
660 Omicron virus causes attenuated disease in mice and hamsters. Nat 2022 6037902
661 603:687–692.

662 29. Stewart R, Yan K, Ellis SA, Bishop CR, Dumenil T, Tang B, Nguyen W, Larcher T, Parry
663 R, Sng JDJ, Khromykh AA, Sullivan RKP, Lor M, Meunier FA, Rawle DJ, Suhrbier A.
664 2023. SARS-CoV-2 omicron BA.5 and XBB variants have increased neurotropic
665 potential over BA.1 in K18-hACE2 mice and human brain organoids. Front Microbiol
666 14.

667 30. Perez-Zsolt D, Muñoz-Basagoiti J, Rodon J, Elousa M, Raïch-Regué D, Risco C, Sachse
668 M, Pino M, Gumber S, Paiardini M, Chojnacki J, Erkizia I, Muñiz X, Ballana E, Riveira-
669 Muñoz E, Noguera M, Paredes R, Trinité B, Tarrés-Freixas F, Blanco I, Guallar V,
670 Carrillo J, Blanco J, Telenti A, Heyn H, Segalés J, Clotet B, Martinez-Picado J, Vergara-
671 Alert J, Izquierdo-Useros N. 2021. Siglec-1 on dendritic cells mediates SARS-CoV-2
672 trans-infection of target cells while on macrophages triggers proinflammatory
673 responses. bioRxiv 8:2021.05.11.443572.

674 31. Rodon J, Muñoz-Basagoiti J, Perez-Zsolt D, Noguera-Julian M, Paredes R, Mateu L,
675 Quiñones C, Perez C, Erkizia I, Blanco I, Valencia A, Guallar V, Carrillo J, Blanco J,
676 Segalés J, Clotet B, Vergara-Alert J, Izquierdo-Useros N. 2021. Identification of
677 Plitidepsin as Potent Inhibitor of SARS-CoV-2-Induced Cytopathic Effect After a Drug
678 Repurposing Screen. Front Pharmacol 12:646676.

679 32. Haagmans BL, van den Brand JMA, Raj VS, Volz A, Wohlsein P, Smits SL, Schipper D,
680 Bestebroer TM, Okba N, Fux R, Bensaid A, Solanes Foz D, Kuiken T, Baumgärtner W,
681 Segalés J, Sutter G, Osterhaus ADME. 2016. An orthopoxvirus-based vaccine

682 reduces virus excretion after MERS-CoV infection in dromedary camels. Science (80-
683) 351:77–81.

684 33. Brustolin M, Rodon J, Rodríguez de la Concepción ML, Ávila-Nieto C, Cantero G,
685 Pérez M, Te N, Noguera-Julián M, Guallar V, Valencia A, Roca N, Izquierdo-Useros N,
686 Blanco J, Clotet B, Bensaid A, Carrillo J, Vergara-Alert J, Segalés J. 2021. Protection
687 against reinfection with D614- or G614-SARS-CoV-2 isolates in golden Syrian
688 hamster. Emerg Microbes Infect 10:797.

689 34. Dowall SD, Graham VA, Tipton TRW, Hewson R. 2009. Multiplex cytokine profiling
690 with highly pathogenic material: use of formalin solution in luminex analysis. J
691 Immunol Methods 348:30–35.

692

693

694

695 **Figure Legends**

696 **Figure 1. Expression of hACE2 in the Col1a1-K18-hACE2 KI model.** (A) Schematic
697 representation of insertion strategy. The original K18-hACE2 transgene was inserted into
698 the collagen COL1A1 locus using a recombinase mediated cassette exchange (RMCE) FLP-
699 FRT system in KH2 cells via blastocyst injection. pPGK-ATG-frt plasmid: vector backbone
700 with Ampicillin resistant gene (Amp), transcription start site (ATG) and Flippase recognition
701 target (Frt). Hygro: Hygromicin resistance gene. pCAGGS-FlpE: expression plasmid for FLPe
702 recombinase expression. (B) Relative quantification of hACE2 receptor expression to GAPDH
703 expression in uninfected Col1a1-K18-hACE2 ((blue empty dot, n=3) and K18-hACE2 males
704 (black empty square, n=3). Delta Ct values are inversely shown to facilitate interpretation.
705 The lower the absolute number, the higher the relative expression. Solid line and bars
706 represent mean and SEM. (C) Relative comparison of hACE2 receptor expression in Col1a1-
707 K18-hACE2 versus K18-hACE2 mice (n=3 each, males). Higher receptor expression in Col1a1-
708 K18-hACE2 (negative values in Y axis) is marked by blue bars, and higher expression in K18-
709 hACE2 (positive values in Y axis) is marked in black bars.

710 **Figure 2. Experimental setting and progression of SARS-CoV-2 infection in Col1a1-K18-**
711 **hACE2 and K18-hACE2 mouse models.** (A) Schematic representation of the experimental
712 setting. Knock-in Col1a1-K18-hACE2 (n=27) and transgenic K18-hACE2 mice (n=4) were
713 intranasally challenged with a 1000 $TCID_{50}$ dose of a B.1 SARS-CoV-2 isolate. A Col1a1-K18-
714 hACE2 uninfected control group (n=5) was challenged with PBS. Mice were monitored for
715 weight-loss and clinical signs for 14 days post infection (dpi). Euthanasia was performed at
716 3, 7, and 14 dpi or upon fulfilment of humane endpoint criteria, for sample and tissue

717 collection (n=8 per timepoint). Infections were performed in two separate experiments
718 between January and June 2022. Created with Biorender.com. (B) Relative body weight
719 follow-up referred to day 0. Col1a1-K18-hACE2 uninfected (blue empty dot), Col1a1-K18-
720 hACE2 infected (blue dot), K18-hACE2 infected (black square). Solid lines and bars represent
721 mean±SD. (C) Survival (Kaplan-Meier). All K18-hACE2 infected animals (n=4) had to be
722 euthanized due to endpoint criteria by 7dpi, and only three infected Col1a1-K18-hACE2 at
723 8, 9, and 10 dpi. No uninfected Col1a1-K18-hACE2 had to be euthanized under this criterion.
724 Col1a1-K18-hACE2 uninfected (blue dashed line), Col1a1-K18-hACE2 infected (blue line),
725 K18-hACE2 infected (black line). Statistical differences were identified using a Log-rank
726 (Mantel-Cox) test (<0.0001), followed by individual comparisons (**p < 0.005; ****p <
727 0.0001)

728 **Figure 3. Progression of SARS-CoV-2 infection in Col1a1-K18-hACE2 KI mice.** Col1a1-K18-
729 hACE2 (blue circles, *n=27*) and K18-hACE2+ mice (black squares, *n=4*) were inoculated with
730 1000 $TCID_{50}$ of a SARS-CoV-2 B.1 isolate (full shapes) or uninfected (empty shapes of each
731 colour, *n=5*). Animals were euthanized at 3dpi (n=8), 7dpi (n=8), 14 dpi (n=8) or upon
732 fulfilment of humane endpoint criteria. (A) SARS-CoV-2 viral RNA loads (copies/mL) of
733 oropharyngeal swab, lung, and nasal turbinate samples. Dashed line represents limit of
734 detection, established by 2SD of uninfected animals. Statistical differences were identified
735 using a Peto-Peto Left censored test (*p < 0.05, **p<0.005). (B) Viral titration of replicative
736 virus ($TCID_{50/}$mL) in lung samples from B.1 infected mice at different endpoints in Vero E6
737 cells on day 5 of culture. Titers were compared using an Independence Asymptotic
738 Generalized Pearson Chi-Squared Test for ordinal data (*p < 0.05, **p<0.005). (C) Lung

739 histopathological scoring of broncho-interstitial pneumonia (left) and SARS-CoV-2 NP
740 immunohistochemical (IHC) scoring (right) in both models at 3, 7, 14 dpi and endpoint.
741 Statistical differences were identified using an Independence Asymptotic Generalized
742 Pearson Chi-Squared Test for ordinal data (*p < 0.05). (D) Representative lung histology and
743 IHC pictures of both models at 3, 7, 14 dpi and endpoint. Images show low-power
744 magnification bars (200 µm).

745 **Figure 4. Inflammatory response in the lung.** The concentration of Inflammatory cytokines
746 in lung extracts in the knock-in and transgenic models at 3,7,14 dpi or endpoint are shown.
747 Col1a1-K18-hACE2 infected (blue full circles, *n=23*), uninfected (blue empty circles, n=3) and
748 K18-hACE2+ infected mice (black full squares, *n=4*). The bar shows Median with
749 interquartile range. Limit of detection for each cytokine is indicated by a dotted line.
750 Statistical differences were identified using a Kruskal Wallis, and a Conover's nonparametric
751 all-pairs comparison test (*p < 0.05, **p<0.005).

752 **Figure 5. Progression of SARS-CoV-2 infection in brain from the Col1a1-K18-hACE2 KI mice.**
753 Col1a1-K18-hACE2 (blue circles, *n=27*) and K18-hACE2+ mice (black squares, *n=4*) were
754 inoculated with 1000 $TCID_{50}$ of a B.1 SARS-CoV-2 isolate (full shapes) or uninfected (empty
755 shapes, *n=5*) and followed until 14 days post infection (dpi). Samples were collected at 3, 7,
756 14 dpi and endpoint. (A) SARS-CoV-2 viral RNA loads (copies/mL) in brain extracts. Dashed
757 line represents limit of detection, established by 2SD of uninfected animals. Statistical
758 differences were identified using a Peto-Peto Left-censored samples test with correction for
759 multiple comparisons. (B) Brain histopathological scoring of multifocal lymphoplasmacytic
760 meningo-encephalitis in brain (Left) and SARS-CoV-2 NP IHC scoring (right) in brain of both

761 models. Statistical differences were identified using an Independence Asymptotic
762 Generalized Pearson Chi-Squared Test for ordinal data (*$p < 0.05$; **$p < 0.01$). (C)
763 Representative images of brain Histology and IHC images of both hACE2+ mouse models.
764 Images show low-power magnification (top; bars: 600µm) and medium-power
765 magnification (bottom; bars: 300µm). Col1a1-K18-hACE2 KI mice samples shown were
766 collected at 7 dpi, while K18-hACE2 samples were collected at humane endpoint (6-7dpi).

767 **Figure 6. Spider Plot of clinical data compilation at 7 dpi from both animal models.**
768 Comparative data summary of Col1a1-K18-hACE2 and K18-hACE2 mice infection by a B.1
769 SARS-CoV-2 isolate. Data at 7dpi of the KI (blue; euthanized at 7 dpi) and K18-hACE2 (black;
770 euthanized at 6-7dpi) of different parameters was compilated and median values are shown
771 in each axis of the spider plot. Data ranges are adjusted for each kind of data, and shown by
772 concentric circles, being the outside circle the highest level. Clinical status was assessed in
773 different categories: respiration, appearance, weight-loss, lack of responsiveness and
774 neurological signs. Histology and IHQ data were semiquantitatively scored from 0-2, 0-3 and
775 0-3 respectively as described in Materials and Methods section. Viral loads are shown as
776 Log10 copies/mL, titration as Log10 TCID50 and cytokines as pg/mL.

A

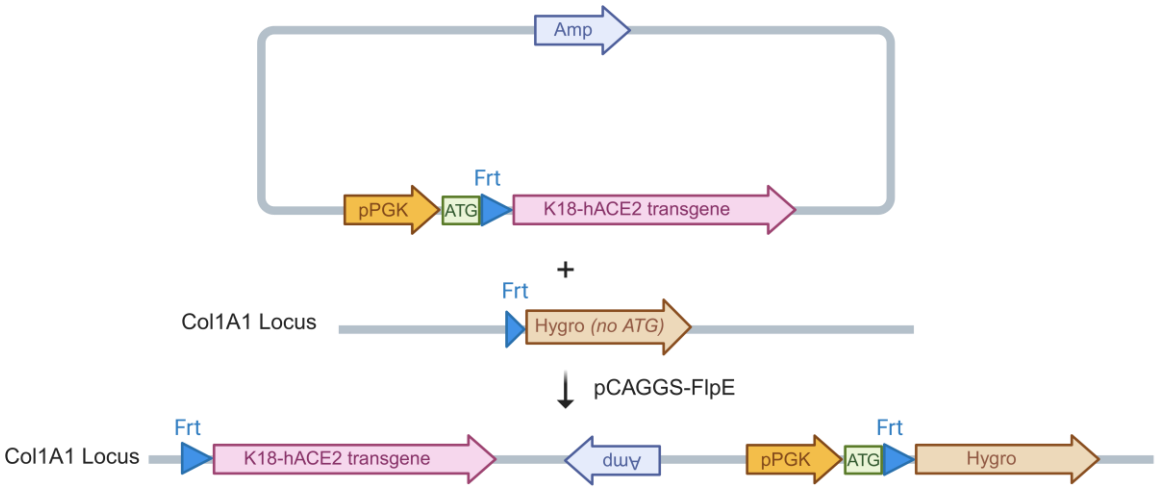
Amp
Frt
pPGK
ATG
K18-hACE2 transgene
+
Frt
Col1A1 Locus
Hygro (no ATG)
pCAGGS-FlpE
Frt
Col1A1 Locus
K18-hACE2 transgene
Amp
pPGK
Frt
ATG
Hygro

B

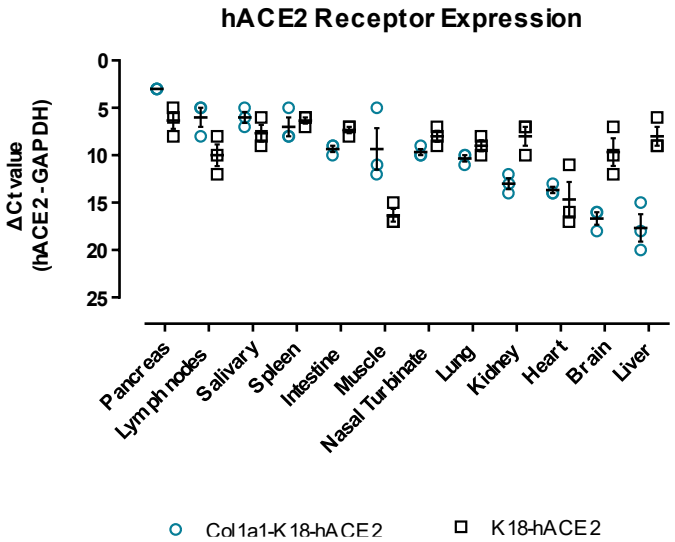
hACE2 Receptor Expression
ΔCt value
(hACE2 - GAPDH)
0
5
10
15
20
25
Pancreas
Lymph nodes
Salivary
Spleen
Intestine
Muscle
Nasal Turbinate
Lung
Kidney
Heart
Brain
Liver
Col1a1-K18-hACE2
K18-hACE2

C

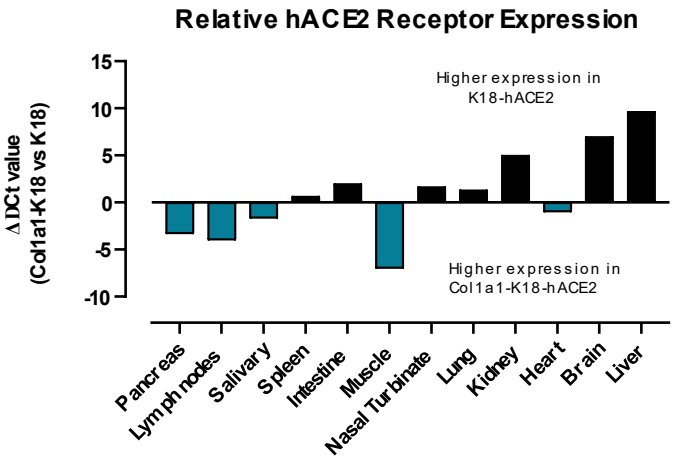
Relative hACE2 Receptor Expression
ΔΔCt value
(Col1a1-K18 vs K18)
15
10
5
0
-5
-10
Higher expression in
K18-hACE2
Higher expression in
Col1a1-K18-hACE2
Pancreas
Lymph nodes
Salivary
Spleen
Intestine
Muscle
Nasal Turbinate
Lung
Kidney
Heart
Brain
Liver

Fig 1.

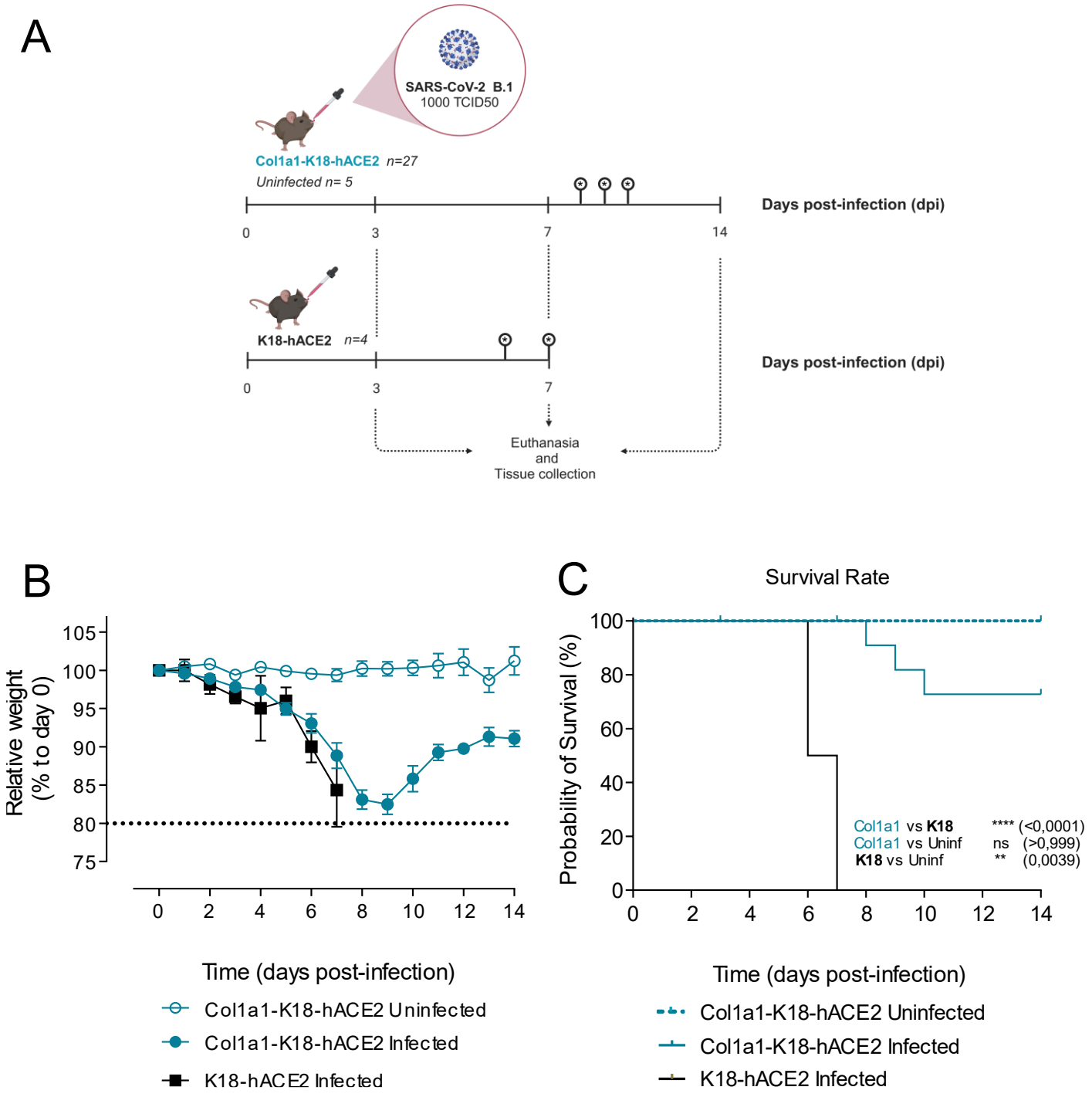
A
SARS-CoV-2 B.1
1000 TCID50
Col1a1-K18-hACE2 n=27
Uninfected n= 5
Days post-infection (dpi)
0
3
7
14
K18-hACE2 n=4
Days post-infection (dpi)
0
3
7
Euthanasia
and
Tissue collection
B
Relative weight
(% to day 0)
105
100
95
90
85
80
75
0
2
4
6
8
10
12
14
Time (days post-infection)
Col1a1-K18-hACE2 Uninfected
Col1a1-K18-hACE2 Infected
K18-hACE2 Infected
C
Survival Rate
Probability of Survival (%)
100
80
60
40
20
0
Col1a1 vs K18 **** (<0,0001)
Col1a1 vs Uninf ns (>0,999)
K18 vs Uninf ** (0,0039)
Time (days post-infection)
Col1a1-K18-hACE2 Uninfected
Col1a1-K18-hACE2 Infected
K18-hACE2 Infected

Fig 2.

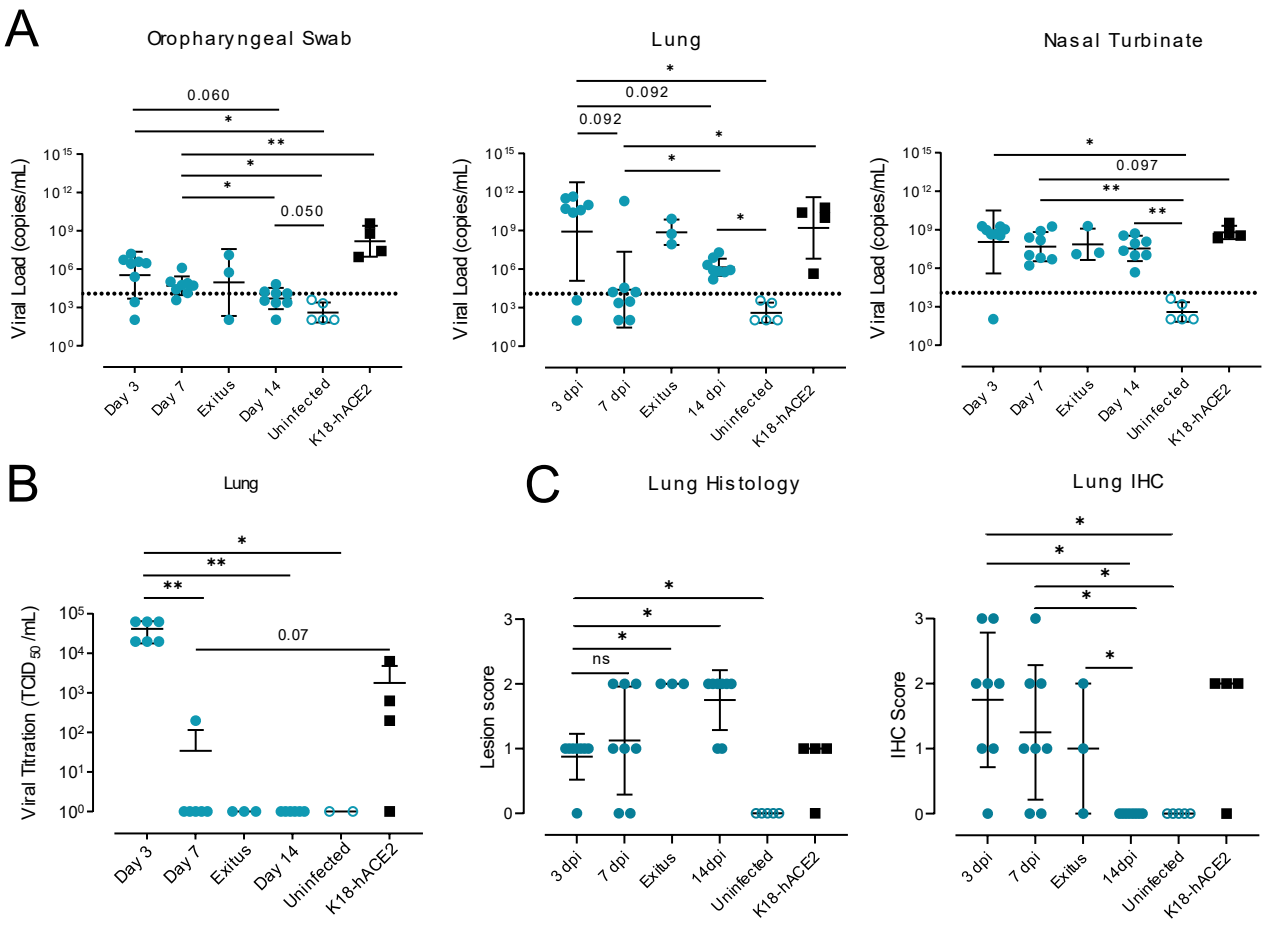
A
Oropharyngeal Swab
Lung
Nasal Turbinate
Viral Load (copies/mL)
Day 3
Day 7
Exitus
Day 14
Uninfected
K18-hACE2
3 dpi
7 dpi
14 dpi
0.060
0.050
0.092
0.097
B
Lung
Viral Titration (TCID50 /mL)
0.07
C
Lung Histology
Lung IHC
Lesion score
IHC Score
ns
14dpi

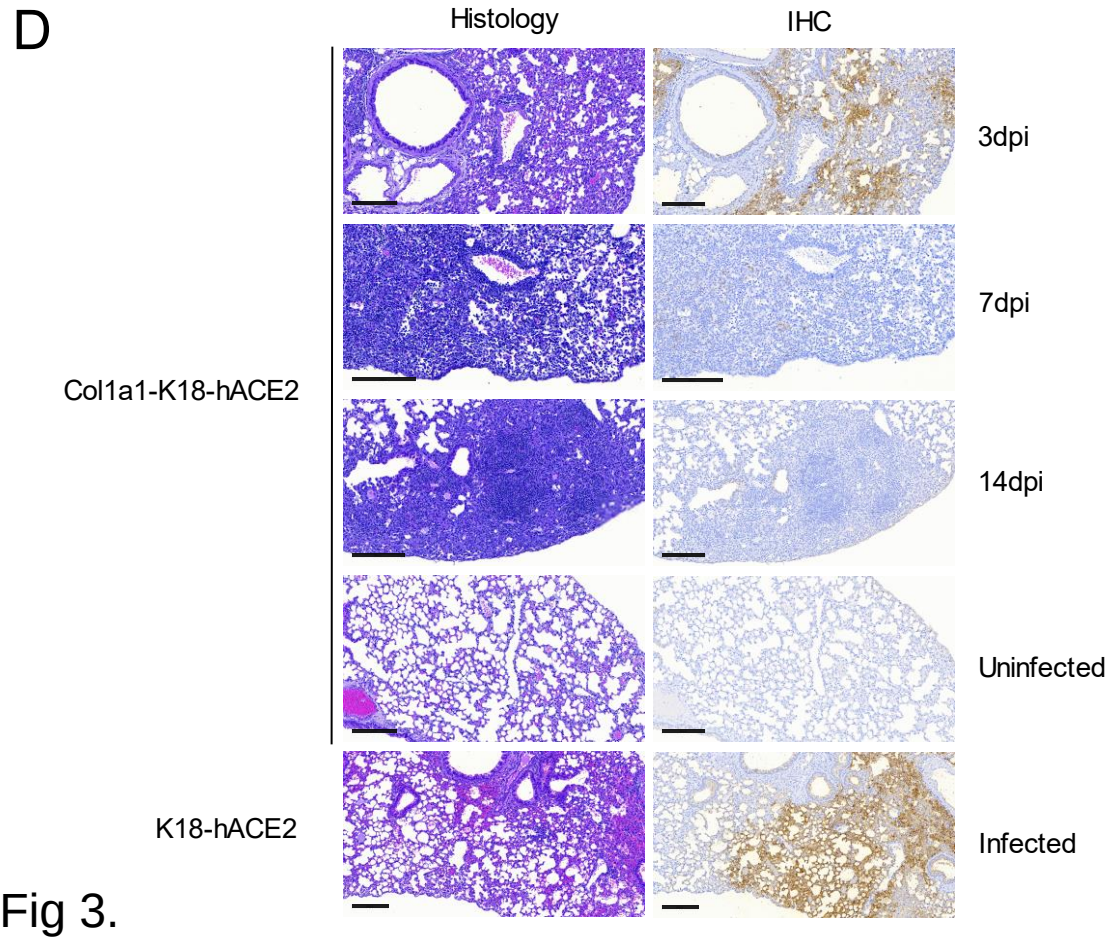
D
Histology
IHC
3dpi
7dpi
14dpi
Uninfected
Infected
Col1a1-K18-hACE2
K18-hACE2

Fig 3.

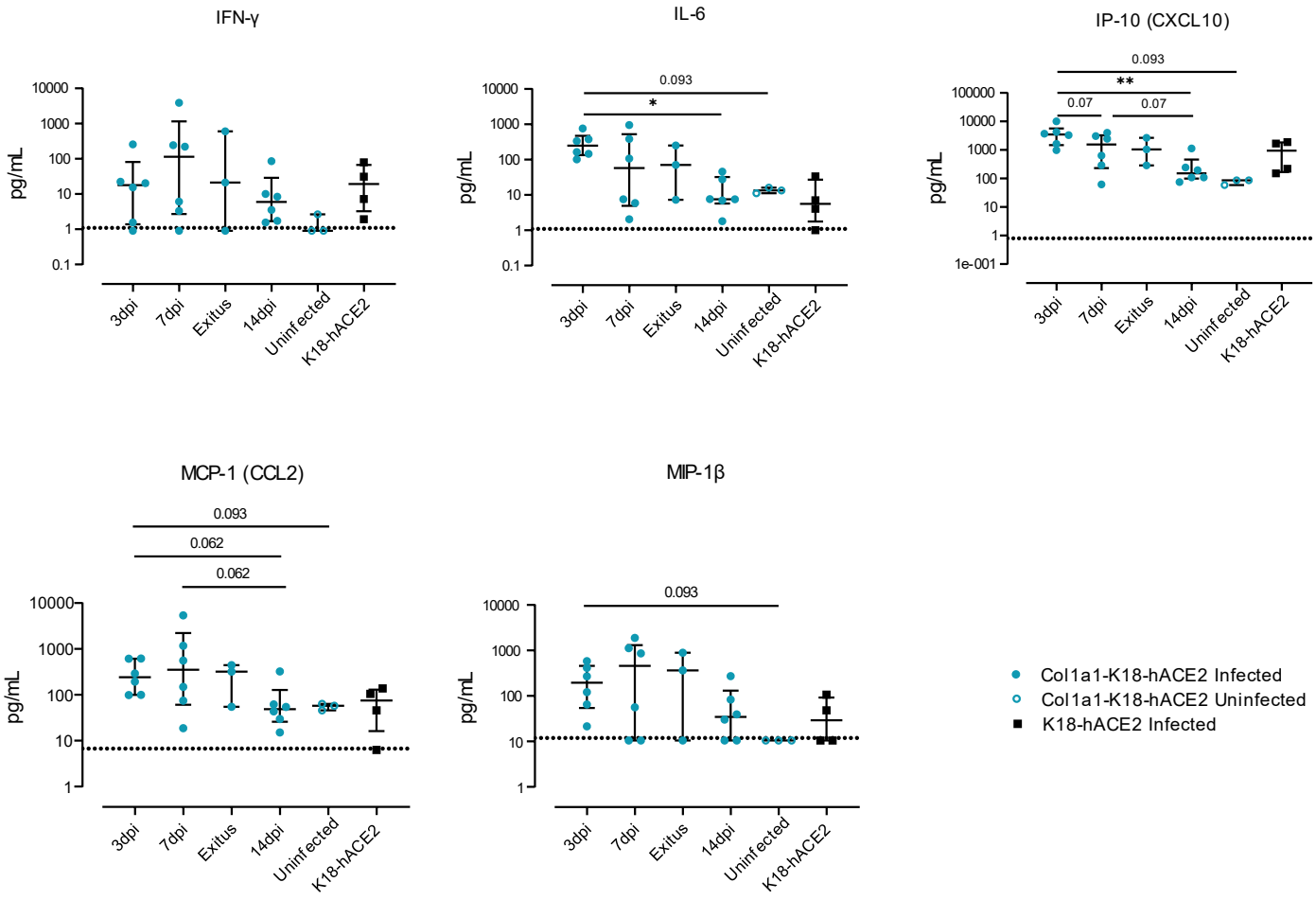
IFN-γ
IL-6
IP-10 (CXCL10)
MCP-1 (CCL2)
MIP-1β
pg/mL
3dpi
7dpi
Exitus
14dpi
Uninfected
K18-hACE2
0.093
*
**
0.07
0.062
Col1a1-K18-hACE2 Infected
Col1a1-K18-hACE2 Uninfected
K18-hACE2 Infected

Fig 4.

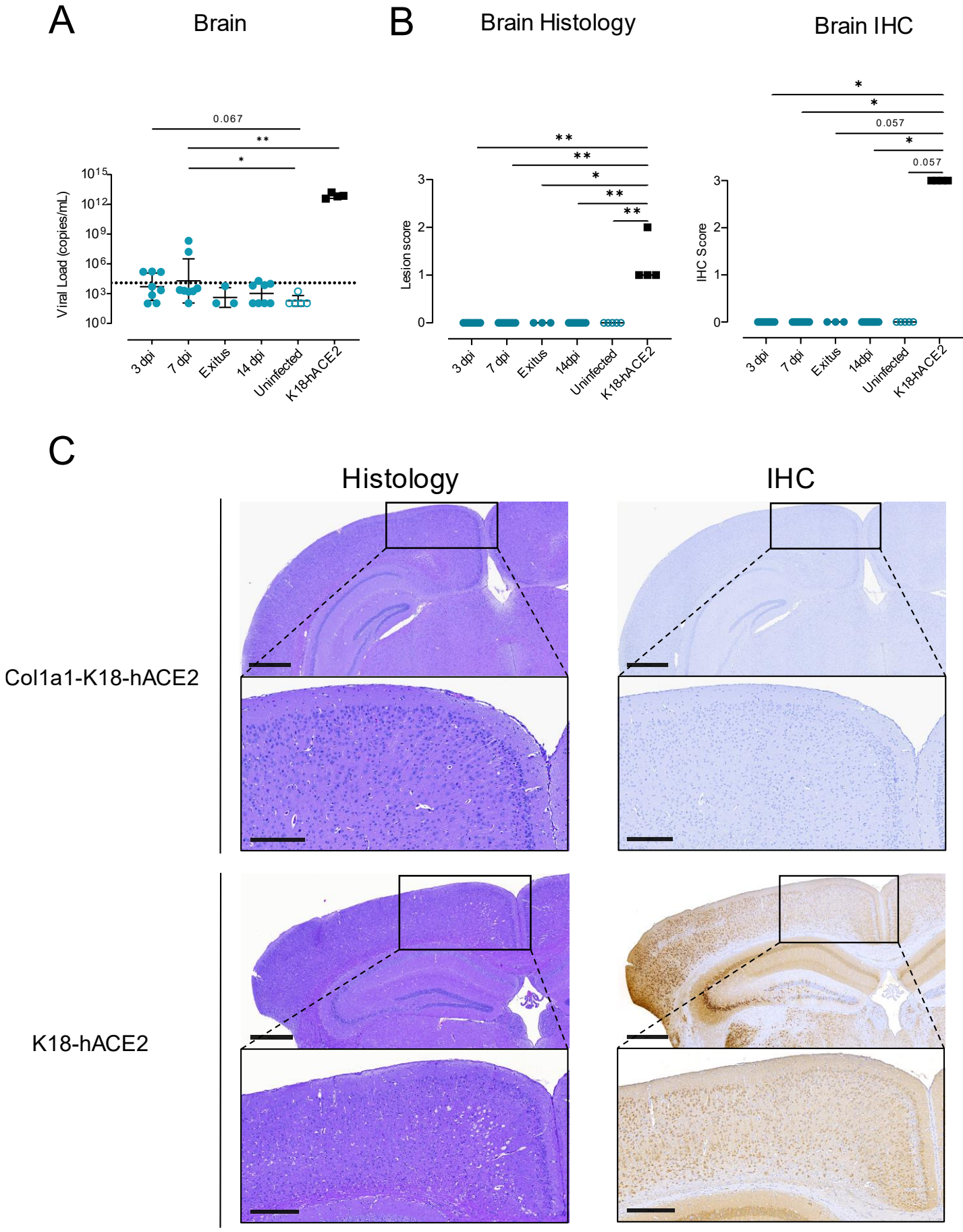
A
Brain
0.067
**
*
Viral Load (copies/mL)
10^{15}
10^{12}
10^{9}
10^{6}
10^{3}
10^{0}
3 dpi
7 dpi
Exitus
14 dpi
Uninfected
K18-hACE2
B
Brain Histology
**
**
*
**
**
Lesion score
0
1
2
3
3 dpi
7 dpi
Exitus
14dpi
Uninfected
K18-hACE2
Brain IHC
*
*
0.057
*
0.057
IHC Score
0
1
2
3
3 dpi
7 dpi
Exitus
14dpi
Uninfected
K18-hACE2
C
Histology
IHC
Col1a1-K18-hACE2
K18-hACE2

Fig 5.

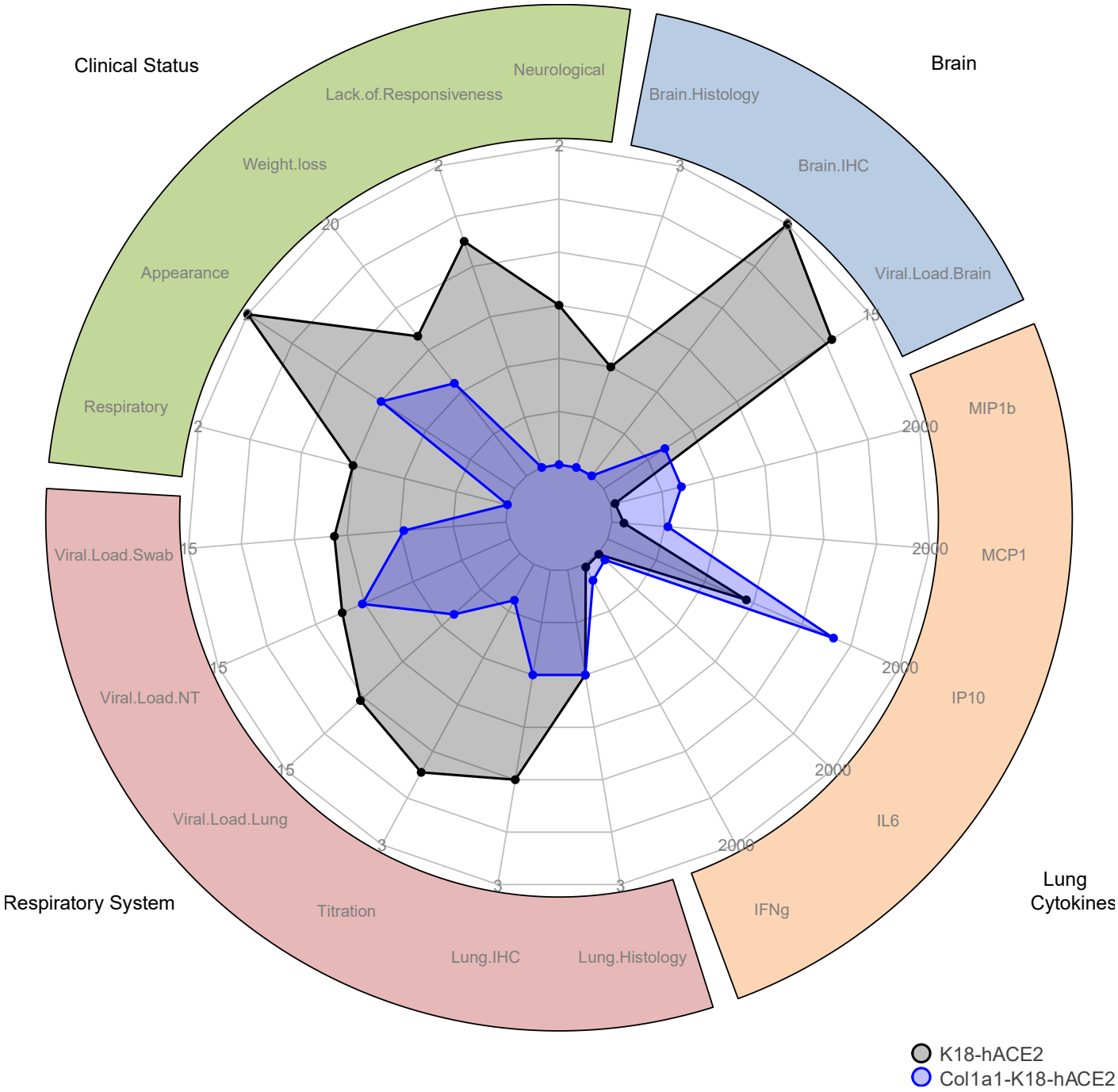
Clinical Status
Neurological
Lack.of.Responsiveness
Weight.loss
Appearance
Respiratory
Brain
Brain.Histology
Brain.IHC
Viral.Load.Brain
Lung Cytokines
MIP1b
MCP1
IP10
IL6
IFNg
Respiratory System
Lung.Histology
Lung.IHC
Titration
Viral.Load.Lung
Viral.Load.NT
Viral.Load.Swab
2
3
15
2000
20
K18-hACE2
Col1a1-K18-hACE2

Fig 6.